



Heat-transfer analysis and thermal dispersion in thermally-developing region of a sintered porous metal channel

W.H. Hsieh*, S.F. Lu

Department of Mechanical Engineering, National Chung Cheng University, Chia Yi 621, Taiwan

Abstract

The thermal dispersion and heat-transfer processes in the thermally-developing region of a sintered porous metal channel with asymmetric heating are analyzed by a two-equation model. The two-equation model considers different energy equations for the bronze and air due to the large difference in their thermal conductivities. In order to account for the large heat-transfer characteristics caused by the growth of thermal boundary layer in the thermal entrance region, the thermal dispersion conductivity is modeled as the product of an entrance-effect function, the dispersive length and the Peclet number. The empirical coefficients in the entrance-effect function are determined by comparing the experimental data. From the calculated results it is found a two-equation model underpredicts the Nusselt number if the thermal-entrance effect function is not included in the model. A parametric study is also conducted to investigate the effect of Peclet number and thermal conductivity ratio on the calculated Nusselt number distribution. © 2000 Elsevier Science Ltd. All rights reserved.

Keywords: Porous media; Thermally-developing region; Forced convection; Thermal dispersion

1. Introduction

Due to its augmented heat and mass transfer, porous media has been widely applied in various industrial applications such as chemical catalytic beds, electronic cooling, high-efficiency heat exchangers, etc. The heat transfer augmentation of porous media is mainly caused by the thermal dispersion of the fluid and the large contact-surface area between the solid matrix and the fluid. In the applications of electronic cooling and heat exchanges, porous materials with large thermal conductivity, such as bronze, copper, aluminum, and

other metals, are usually adopted to enhance the heat transfer efficiency.

In a recent paper by Hsu and Cheng [8], the modeling of thermal dispersion was surveyed in detail and the thermal dispersion conductivity tensor for convection in a porous medium was derived based on the method of volume averaging of the velocity and temperature deviations in the pores. According to Hsu and Cheng [8], the effect of thermal dispersion on the forced convection in porous media has been well documented in the chemical engineering literature [2,14,15,21,22]. In these studies, the transverse or radial thermal dispersion conductivity was correlated as a function of Peclet number, i.e.

$$\frac{k_t^*}{k_f} = D_T Pe_m \quad (1)$$

* Corresponding author. Tel.: +886-5-2428170; fax: +886-5-2720589.

E-mail address: imewhh@ccunix.ccu.edu.tw (W.H. Hsieh).

ing for the wall effect on the thermal dispersion conductivity and u/u_m was introduced to account for the local volume-averaged velocity variation. From their studies, Cheng et al. [3] concluded that the use of a van Driest type wall function in Eq (4) is necessary to reproduce theoretically the steep temperature gradient observed in the experiment conducted by Schroeder et al. [16].

In these studies, the constants, D_T , γ and w in Eqs. (1)–(4) were determined by matching experimental data. In the past, the experimental data adopted for the determination of these constants were either the Nusselt number for thermally fully-developed flows [21,22] or the temperature distribution at a particular axial location [16]. Therefore, none of the existing correlations of thermal dispersion was developed from the experimental data of the thermally-developing region of porous media. In addition, none of these studies were conducted for metal porous media. As a result, very little attention was paid to the study of heat transfer processes in the thermally-developing region of porous materials with large thermal conductivity, and the study of thermal dispersion in thermally-developing regions remains inadequate.

In the use of porous media for the application of high-performance heat exchangers, the length of the flow passage of a heat exchanger is often short. Under such circumstances, the thermal-entrance region occupies a significant portion of the total length of the flow passage of a heat exchanger, and therefore, the effect of thermal-entrance region should be considered. In this work, the heat transfer and thermal dispersion in the thermally-developing region of a sintered bronze porous annulus are studied with a two-equation model. The two-equation model considers different energy equations for the bronze (with large thermal conductivity) and air due to the large difference in their thermal conductivities. A thermal-entrance effect function is included in the modeling of thermal dispersion to account for the enhanced heat-transfer characteristics of the fluid caused by the growth of the thermal boundary layer in the thermally-developing region. The empirical constants in the thermal-entrance effect function are determined by comparing with experimental data of Hwang and Chao [10], in which the axial wall temperature distributions in a hydraulically fully-developed, thermally-developing porous channel are measured under different heating and Reynolds number conditions. The goal of this work is to develop an empirical correlation of the thermal dispersion conductivity for the thermally-developing region of a metal porous channel with large thermal conductivity. In addition, the heat transfer processes in the thermally-developing region are also studied.

2. Theoretical approach

The theoretical model of this work considers hydraulically fully-developed, thermally-developing air flowing through a sintered brass channel with asymmetric heating to simulate the experimental condition of Hwang and Chao [10]. The channel height is 1 cm. The top wall of the channel is thermally insulated and the bottom wall is subjected to constant heat-flux boundary condition (see Fig. 1). The momentum equation based on the Brinkman–Darcy–Ergun model [3,8–10] for hydraulically fully-developed region is

$$-\frac{dp}{dx} = \frac{\mu}{K}u + \frac{\rho_f F}{\sqrt{K}}u^2 - \frac{\mu}{\varepsilon} \frac{d^2u}{dy^2} \quad (5)$$

where ε is the porosity of the sintered brass channel, u the volume-averaged local velocity (also termed seepage velocity, filtration velocity or superficial velocity), K the permeability, and F the inertia coefficient.

In modeling the heat-transfer processes, most of the research work done in the past adopted the local thermal equilibrium assumption to combine the energy equations for the solid matrix and the fluid into a single one. However, in their study of the convective heat transfer in a sintered brass channel, Hwang and Chao [10] showed that it was necessary to use a two-equation model to correctly predict the Nusselt number under the condition of large difference in the solid and fluid thermal conductivities. In this work, the volume-averaging is applied to the solid and the fluid to obtain the following two energy equations. [1].

$$0 = h_{\text{loc}}a(T_f - T_s) + \frac{\partial}{\partial y} \left(k_s^* \frac{\partial T_s}{\partial y} \right) \quad (6)$$

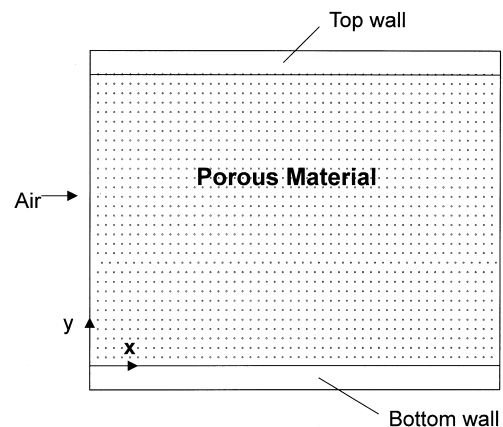


Fig. 1. Schematic diagram of the physical model.

$$\begin{aligned} & \rho_f C_{Pr} u \frac{\partial T_f}{\partial x} + \rho_f C_{Pr} v \frac{\partial T_f}{\partial y} \\ & = h_{loc} a (T_s - T_f) + \frac{\partial}{\partial y} \left[(k_f^* + k_t^*) \frac{\partial T_f}{\partial y} \right] \end{aligned} \quad (7)$$

where k_s^* is the stagnant thermal conductivity of the solid, k_f^* the effective thermal conductivity of the fluid, h_{loc} the internal convective heat-transfer coefficient between the solid and the fluid, a the specific interface surface area per unit volume ($= 20.34 (1 - \varepsilon) \varepsilon^2 / d$ [10,12]). k_s^* and k_f^* are considered to be functions of temperature in this study. The convective heat transfer coefficient, h_{loc} , has been determined experimentally by various researchers [12,13,17,20] and is modeled as

$$h_{loc} = c_h Re^{n_h} Pr^{m_h} \quad Re = \frac{\rho_f a d}{\mu} \quad (8)$$

where c_h , n_h and m_h are empirical constants and their values are 0.004, 1.35, and 0.333, respectively, for $Re \leq 100$, and 0.0156, 1.04, 0.333 for $Re > 100$.

The effective thermal dispersion conductivity, k_t^* , responsible for the heat transfer introduced by the velocity deviation caused by the solid matrix, is related to the Peclet number, the dispersive length, and an entrance-effect function.

$$\frac{k_t^*}{k_f} = D_T Pe \ell E \quad (9)$$

where Pe is the Peclet number based on the volume-averaged local velocity, ℓ is the dispersive length given in Eq. (4) and E is the entrance-effect function, which accounts for the enhanced thermal dispersion caused by the growth of thermal boundary layer in the thermally-developing region. The entrance effect function is expressed as

$$E = 1 + C_e [x/L_{ent}]^{-n_e / Re_0} \quad (10)$$

where L_{ent} is the characteristic length scale of the thermal entrance region which is proportional to the Prandtl number and Reynolds number based on the entrance fluid velocity and the height of the flow passage, C_e and n_e are empirical constants. The form of the entrance-effect function is determined by the following phenomenological considerations. In Eq. (10), (x/L_{ent}) represents the ratio of axial distance to the scale of thermal entrance length. Based on Eq. (10), the entrance function is inversely proportional to the ratio of the axial distance to thermal entrance length. At the axial location where (x/L_{ent}) is small, i.e. the region where thermal boundary layer just started to grow, the value of entrance effect function is large to account for the strong thermally-developing effect. When the flow is thermally fully developed, the value

of entrance-effect function approaches unit and its effect diminishes.

In closing the model, the ideal-gas equation of state and mass conservation equation for the fluid adopted in the model are given below.

$$p = \rho_f R T_f \quad (11)$$

$$\int \rho_f u \, dA = \rho_o u_o A \quad (12)$$

$$\frac{\partial(\rho_f u)}{\partial x} + \frac{\partial(\rho_f v)}{\partial y} = 0 \quad (13)$$

Eqs. (5)–(7) and (11)–(13) can be nondimensionalized by introducing the following dimensionless variables:

$$\bar{x} = x/H \quad \bar{y} = y/H \quad \bar{u} = u/u_0 \quad \bar{p} = p/\rho_f u_0^2$$

$$\bar{H} = H/d \quad \bar{T}_s = T_s/T_0 \quad \bar{T}_f = T_f/T_0 \quad \bar{\rho}_f = \rho_f/\rho_{f0}$$

$$D_A = \frac{K}{H^2} \quad Pr_f = \frac{C_{Pr} \mu}{(k_f^* + k_t^*)} \quad Re_d = \frac{\rho_f u_0}{\mu} \quad C_d = ad$$

$$Pe_f = Pr_f Re_d \quad Nu_d = \frac{h_{loc} d}{(k_f^* + k_t^*)} \quad \bar{k}_R = \frac{k_f^* + k_t^*}{k_s^*} \quad (14)$$

After non-dimensionalization, Eqs. (5)–(7) and (11)–(13) become:

$$\begin{aligned} -\frac{d\bar{p}}{d\bar{x}} &= \left(\frac{1}{\bar{H} Re_d D_A} \right) \bar{u} + \left(\frac{F}{\sqrt{D_A}} \right) \bar{u}^2 \\ &\quad - \left(\frac{1}{\varepsilon \bar{H} Re_d} \right) \frac{d^2 \bar{u}}{d\bar{y}^2} \end{aligned} \quad (15)$$

$$0 = Nu_d \bar{k}_R C_d \bar{H}^2 (\bar{T}_f - \bar{T}_s) + \frac{d^2 \bar{T}_s}{d\bar{y}^2} \quad (16)$$

$$\begin{aligned} & \left(\bar{u} \frac{\partial \bar{T}_f}{\partial x} + \bar{v} \frac{\partial \bar{T}_f}{\partial y} \right) \\ & = \frac{Nu_d C_d \bar{H}}{Pe_f} (\bar{T}_s - \bar{T}_f) + \frac{\partial}{\partial \bar{y}} \left[\left(\frac{1}{Pe_f \bar{H}} \right) \frac{\partial \bar{T}_f}{\partial \bar{y}} \right] \end{aligned} \quad (17)$$

$$\frac{\partial(\bar{\rho}_f \bar{u})}{\partial \bar{x}} + \frac{\partial(\bar{\rho}_f \bar{v})}{\partial \bar{y}} = 0 \quad (18)$$

$$\bar{p} = \frac{\bar{T}_f}{(\kappa M_0^2)} \quad (19)$$

$$\frac{1}{A} \int \rho_f \bar{u} dA = 1 \tag{20}$$

When the bottom wall is at constant heat-flux condition, the boundary conditions are:

$$\text{at } \bar{y} = 0 \quad \bar{u} = 0 \quad \bar{v} = 0$$

$$\frac{k_s^* T_0}{Hq} \frac{\partial \bar{T}_s}{\partial \bar{y}} + \frac{(k_f^* + k_t^*) T_0}{Hq} \frac{\partial \bar{T}_f}{\partial \bar{y}} = -1$$

$$\text{at } \bar{y} = 1 \quad \bar{u} = 0 \quad \frac{\partial \bar{T}_s}{\partial \bar{y}} = \frac{\partial \bar{T}_f}{\partial \bar{y}} = 0 \tag{21}$$

Governing equations (15)–(20) with boundary conditions are solved numerically for the velocity, the fluid and solid temperatures, the fluid density, and the pressure. Based on the definition of Nusselt number, the local Nusselt number can be deduced from the following equation:

$$Nu_x = \frac{\left[(k_f^* + k_t^*) \frac{\partial T_f}{\partial y} \Big|_{y=0} + (k_s^*) \frac{\partial T_s}{\partial y} \Big|_{y=0} \right] 2H}{k_f^* (T_w - T_0)} \tag{22}$$

where T_0 is the entrance temperature of the fluid.

In solving the governing equations, the governing equations in the physical plane of the problem are transformed into a new set of governing equations in a computational plane according to the following transformation equations.

$$x = \zeta$$

$$y = \frac{H}{2}(1 - \cos \eta)$$

The transformation allows the setup of finely spaced grid in the y -direction near the top and bottom walls in the physical plane, while maintain a uniform grid in the computational plane. Central difference for y -direction and backward difference for x -direction are adopted to discretize Eqs. (15)–(17) and form a tridiagonal system of finite-difference equations. The set of tridiagonal finite-difference equations is solved numerically by a standard matrix solver. Eq. (18) is solved in its integral form to obtain v .

Before Eqs. (15)–(18) are solved numerically, a pressure drop is guessed. Eqs. (15)–(18) are then solved to obtain converged fluid and solid properties. These fluid properties are substituted into Eq. (20) to check the conservation of mass. If not, the value of pressure drop is adjusted until Eq. (20) is satisfied within 0.01%. The criterion of convergence for Eqs. (15)–(18) is

$$\frac{1}{N} \sum_{i=1}^N \left\{ 0.4 \left| \frac{\bar{T}_{f,i}^{k+1} - \bar{T}_{f,i}^k}{\bar{T}_{f,i}^k} \right| + 0.4 \left| \frac{\bar{T}_{s,i}^{k+1} - \bar{T}_{s,i}^k}{\bar{T}_{s,i}^k} \right| + 0.1 \left| \frac{\bar{u}_i^{k+1} - \bar{u}_i^k}{\bar{u}_i^k} \right| + 0.1 \left| \frac{\bar{v}_i^{k+1} - \bar{v}_i^k}{\bar{v}_i^k} \right| \right\} \leq 10^{-5} \tag{23}$$

The determination of the values of weights of relative errors for \bar{T}_f , \bar{T}_s , \bar{u} , and \bar{v} is based on the following considerations: (1) One of the major work items of this study is to calculate the Nusselt number distributions along the axial direction at different Reynolds numbers. Since the Nusselt number is directly linked and most sensitive to the temperature profiles, the weights of relative errors for \bar{T}_f and \bar{T}_s are set larger than those for \bar{u} and \bar{v} . (2) During the numerical calculation, it is noted that \bar{u} and \bar{v} can easily achieve their converged values, but not \bar{T}_s and \bar{T}_f . As a result of this fact, larger weights of the relative errors for \bar{T}_f and \bar{T}_s are set to assure the convergence of the calculation.

To assure the accuracy of the computer program, the calculated flow and solid properties are substituted back into the governing equations (Eqs. (15)–(20)) to compute the relative residual of each equation. The relative residual of each equation is less than 10^{-7} . The overall energy conservation is examined and found to be within 1%. The grid-independent test is also conducted to determine the proper number of grid points in the axial and transverse directions.

3. Results and discussion

3.1. Verification of theoretical model

In order to verify the simulation accuracy of the theoretical model and numerical code developed in this study, a theoretical calculation is performed to simulate the heat-transfer processes of water in a variable-porosity channel packed with glass spheres under asymmetric heating conditions. The calculated results are compared with measured [16] and calculated [3] transverse temperature and velocity profiles at different Reynolds numbers.

Since the goal of this part of the work is to verify the simulation accuracy by comparing the calculated results from this work with the works by Cheng et al. [3] and Shroeder et al. [16], the theoretical model given in Section 2 is modified according to Cheng et al.'s [3] work. In the modification, the energy equations for the solid and fluid are combined into a single energy equation via the assumption of local thermal equilibrium. The porosity is considered to be variable and empirical correlations given below [3] are used to calculate the porosity distribution.

$$\varepsilon = \varepsilon[1 + C_1 \exp(-N_1 y/\gamma_1)] \quad 0 \leq y \leq H/2$$

$$\varepsilon = \varepsilon\{1 + C_1 \exp[-N_1(H-y)/\gamma_1]\} \quad H/2 \leq y \leq H \quad (24)$$

All input data and boundary conditions are the same as those in the works of Cheng et al. [3] and Shroeder et al. [16].

Fig. 2 shows the calculated velocity distributions compared with those from Cheng et al. [3] for $Re = 100$ and 10 . It is seen that the comparison is in good agreement. The velocity increases drastically from the wall to a location near the wall; then it decays gradually. This so-called "channelling effect" in the velocity field is caused by the large variation in porosity near the wall region. This large variation in porosity is considered in the model via the use of Eq. (24) for the determination of the porosity distribution within the packed channel.

Fig. 3 shows the comparison of calculated temperature distributions from this work and those from Cheng et al. [3] and Shroeder et al. [16]. The comparison of the calculated temperature distributions from the present work and Chen, et al. [3] shows good agreement. The calculated temperature distributions are in reasonable agreement with the experimental data of Shroeder et al. [16]. The slight discrepancy between the calculated results (from Chen et al. [3] and the present work) and the experimental data by Shroeder et al. [16] may be attributed to the fact that the porosity distribution of the porous material used in the experimental work of Schroeder et al. was not measured. And therefore, the porosity distribution calculated by Eq. (24) may deviate from the actual porosity distribution of the experiment.

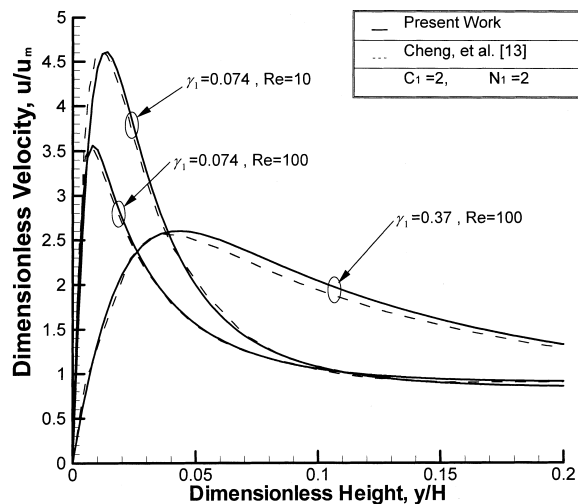


Fig. 2. Comparison of calculated velocity distributions from present work and Cheng et al. [13].

In order to simulate correctly the steep temperature gradient near the wall region, the wall function given in Eq. (4) is adopted in the analysis. It should be noted that in order to obtain good agreement between the measured and calculated temperature data, the empirical constants D_T and w should be adjusted according to the value of N_1 used in the analysis [3]. The values of D_T , w , and N_1 used in the analysis are the same as those of Cheng et al. [3]. From Figs. 2 and 3, it is seen that the calculated velocity and temperature distributions from the model and numerical code developed in this work compare well with previous works. The channelling effect in the velocity distribution and steep temperature gradient near the wall can be successfully simulated by the model and computer code.

3.2. Determination of empirical constants in the entrance-effect function

To determine the empirical constants in the entrance-effect function, the calculated results from the theoretical model and numerical code of this work are compared with the measured experimental data for the thermal-entrance region (the flow is hydraulically fully-developed) of a $5 \times 5 \times 1$ cm porous channel [10]. The porous material is made of sintered bronze beads with a mean diameter, $d = 0.72$ mm. The top and the bottom walls of the porous channel are at adiabatic and constant heat flux conditions, respectively. The values of various parameters used in the analysis are given in Table 1.

Simulation of the heat-transfer processes is first car-

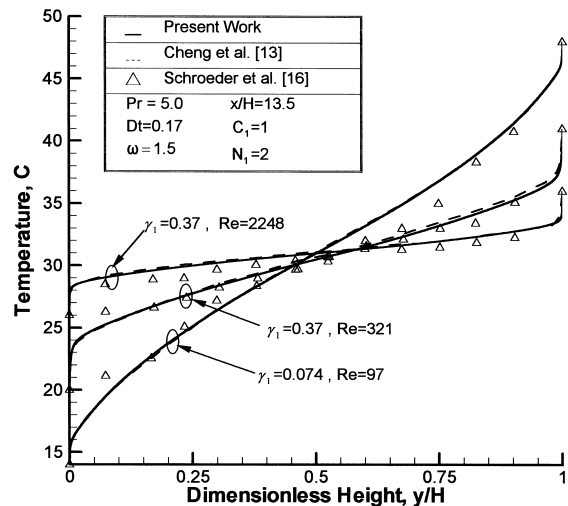


Fig. 3. Comparison of temperature distributions from present work (calculation), Cheng et al. [13] (calculation), and Shroeder et al. [16] (experimental data).

ried out for the thermally-developed region ($x/H \geq 1.755$, based on Hwang and Chao [10]) of the sintered porous channel. In the simulation, the entrance-effect function is set to 1 ($E = 1$) to eliminate its effect. Different values of D_T are used in the simulation. It is found that with $D_T = 0.375$, the predicted temperatures at the bottom wall best match the experimental data for the thermally-developing region under different Reynolds numbers and constant heat-flux conditions.

After the value of D_T is determined, calculations of the heat-transfer characteristics are performed with different values of C_e and n_e . The calculated temperature distributions are then compared with the measured data for thermally-developing region [10]. The values of C_e and n_e are selected based on the best match between the calculated and measured temperature distributions. For $D_T = 0.75$, it is found that the calculated temperature distributions based on $C_e = 0.63$ and $n_e = 125.4$ best match the experimental measurements as shown in Fig. 4. In this process, it is noted if the thermal-entrance effect function is not adopted in the modeling of thermal dispersion conductivity, a good match between the calculation and experimental data in the thermal-entrance region cannot be obtained. It would over-predict wall temperature distributions in thermal-entrance regions. This point will be further discussed in Fig. 7.

From Fig. 4, it is noted that the axial temperature gradient at the bottom wall increases with increasing heat-flux level. This is due to the fact that at higher heat-flux conditions, more heat per unit axial length is transferred to the porous channel and introduces greater temperature rise. On the other hand, the increase in Reynolds number decreases the axial temperature gradient at the bottom wall, which is caused by the stronger cooling effect of the air at higher Reynolds numbers. Fig. 4(c) and (d) show some crossovers of various temperature distributions (which are well simulated by the theory). This is caused by different inlet air temperatures during experiments. For

example, in Fig. 4(c), the inlet air temperature for $Re = 109$ is lower than that for $Re = 154$. The temperature gradient for $Re = 109$, however, is greater than $Re = 154$. As a result of lower inlet air temperature and higher temperature gradient for $Re = 109$, a crossover exists at $x/H \approx 0.4$.

3.3. Heat transfer characteristics in the thermally-developing region

After empirical constants for the thermal-entrance effect function have been determined by comparing experimental data, the calculated solid and fluid temperature distributions at different axial locations are given in Fig. 5 for $Re = 109$, $q = 16 \text{ kW/m}^2$. From Fig. 5, it can be seen that near the bottom wall, the temperature gradient of the fluid is significantly larger than that of the solid due to the large difference in their thermal conductivities. It is also noted that the dimensionless temperature profiles of the solid remain the same at the six axial locations shown in Fig. 5. This indicates the solid phase has a very short thermal entrance length. It should be noted, however, that the “temperature” of the solid phase actually varies significantly in the axial direction when it is converted from a dimensionless to a dimensional quantity. On the other hand, the dimensionless temperature profile of the fluid varies along the axial direction, and it approaches the profile at $x/H = 5.0$.

The calculated temperature difference between the solid and the fluid is given in Fig. 6. It is noted that there is a significant temperature difference between the solid and the fluid due to the large difference in their thermal conductivities. This phenomenon of temperature difference between phases was also observed by Amiri and Vafai [23] and Amiri et al. [24] in their studies of forced convective incompressible flow through porous beds under constant wall temperature or constant heat flux conditions. The location of maximum temperature difference moves away from the heated wall along the axial direction. At $x/H > 1.0$, the location of the maximum temperature difference is at the top wall location due to the fact that the flow has become thermally fully developed.

Fig. 7 shows the comparison of calculated axial distributions of Nusselt number using six different models. Models 1–3 are one-equation models, in which the local thermal equilibrium assumption is adopted, and therefore $T_s = T_f$ and Eqs. (6) and (7) are combined into a single equation. In model 1, the thermal dispersion conductivity, k_t^* , is modeled as given in Eq. (9). In model 2, the thermal dispersion conductivity is modeled as in model 1 but the thermal-entrance effect function, E , is set to unit. In model 3, the thermal dispersion conductivity is set to

Table 1
Input data used in the numerical calculation

Parameter (unit)	Value	Parameter (unit)	Value
C_p (J/kg K)	1007	n_e	95
C_e	0.47	P_0 (Nt/m ²)	1.366
D_T	0.375	R (J/kg K)	288
d (mm)	0.72	T_0 (K)	303.5
ε	0.37	u_0 (m/s)	3.643
F	0.242	w	1.5
H (m)	0.01	ρ_0 (kg/m ³)	1.563
q (W/m ²)	0.8E–4–3.2E–4	μ (N s/m ²)	184.6E–7
K (m ²)	2.9E–10		

zero. Models 4–6 are two-equation models, in which different energy equations are considered for the solid and the fluid. Model 4 is the model developed in this work. In terms of modeling of thermal dispersion conductivity, model 4 is the same as model 1, model 5 the same as model 2, and model 6 the same as model 3. Fig. 7 shows that the calculated Nusselt numbers from one-equation models (models 1–3) are significantly larger than those from the two-equation models (models 4–6). This is due to the fact that the assumption of perfect heat-transfer between the solid and the fluid is adopted in one-equation model. This enhances the heat transfer from the heated wall to the fluid through the solid. It is noted that from the

overlapping of the Nusselt number distributions calculated from models 1–3, it is concluded that the way the thermal dispersion conductivity is modeled does not affect significantly affect the calculated Nusselt number. This is due to the fact that the value of the thermal dispersion conductivity in the energy equation of one-equation model is significantly less than the large thermal conductivity of the solid (bronze) considered in this study. By comparing the calculated Nusselt number distributions from the present model (model 4) and model 5, it is noted that if the thermal-entrance effect function were not included in a two-equation model, the distribution of Nusselt number would be underpredicted.

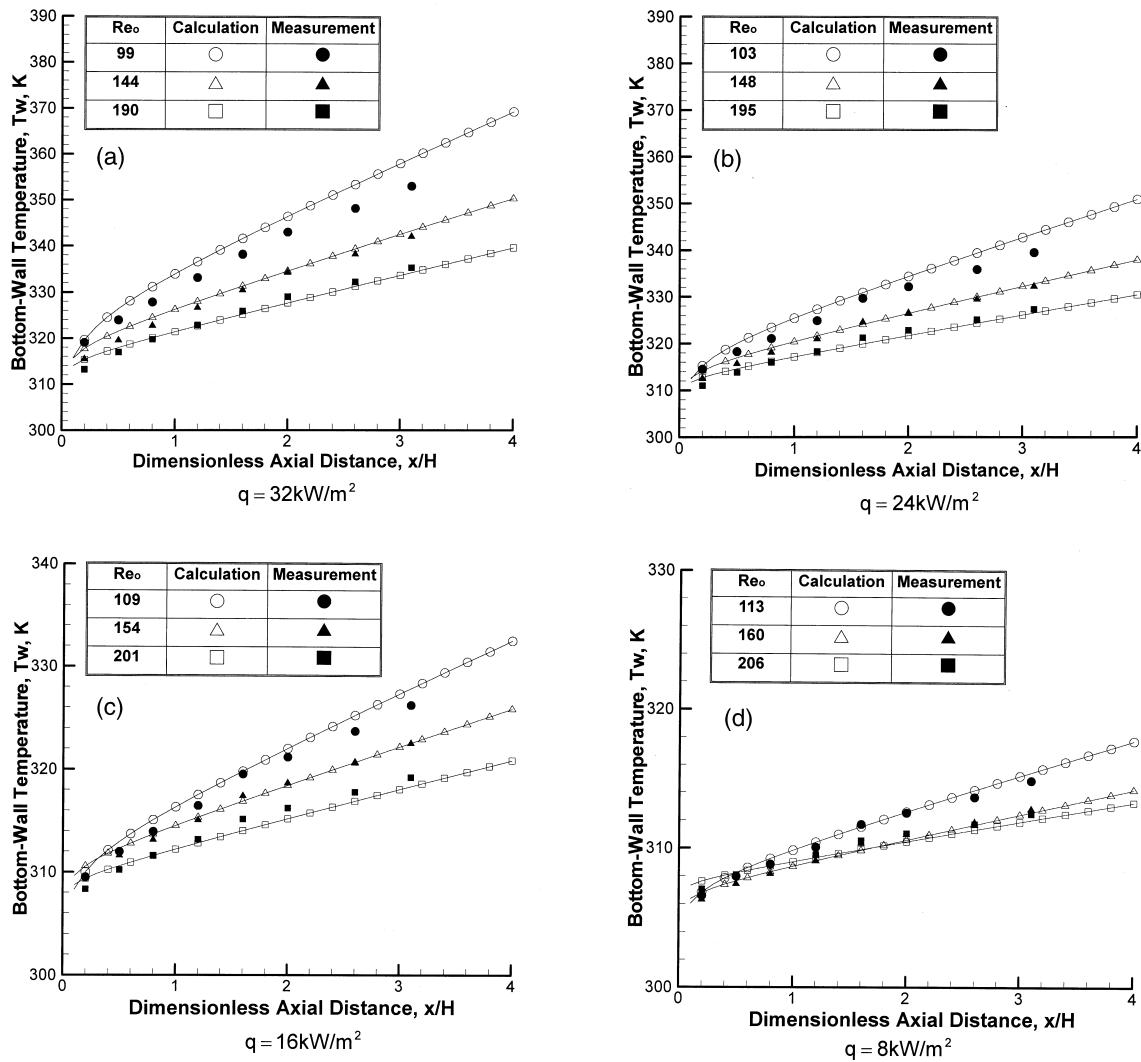


Fig. 4. Comparison of measured and calculated wall-temperature distributions at different Reynolds numbers and heat fluxes. (a) 32 kW/m², (b) 24 kW/m², (c) 16 kW/m², (d) 8 kW/m².

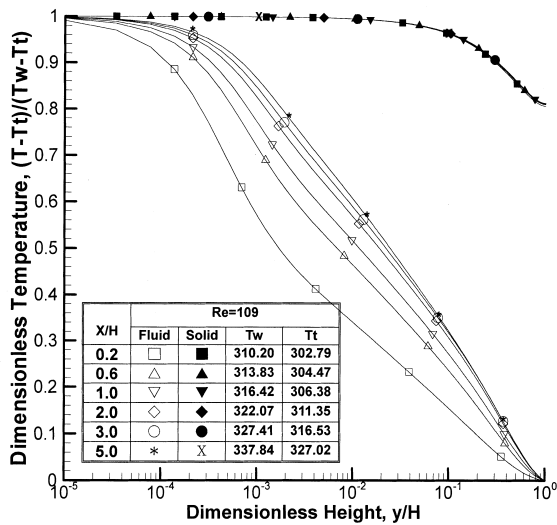


Fig. 5. Calculated dimensionless solid and fluid temperature distributions.

3.4. Effect of thermal conductivity ratio and Peclet number

In this work, a large thermal conductivity material, bronze, was considered as the solid matrix for enhancing the heat transfer. This is different from the applications of chemical catalyst beds, in which low thermal conductivity materials are used as the catalyst beds for enhancing and/or initiating chemical reactions. When analyzing heat-transfer processes in porous media using large thermal conductivity metals, it is imperative to use two-equation models to consider separate energy equations for the solid matrix and the fluid. Fig. 8 shows the effect of the ratio of the thermal conductivity of the fluid to that of the solid on the calculated Nusselt number distributions from one-equation model (model 1 in previous section) and two-equation model (model 4 in previous section). It is seen that at low thermal conductivity ratio ($k_R = k_f/k_s = 5.0E - 4$) similar to the condition that the air flows in the bronze matrix, the calculated Nusselt number distribution from one-equation model is significantly larger than that from two-equation model. As the ratio of thermal conductivity k_R increases the calculated Nusselt number distributions using the two models are getting closer due to the fact that the solid and fluid in the porous channel become more homogeneous under this condition. In the past, several researchers have used different dimensionless variables to investigate the local-thermal-equilibrium (LTE) condition in porous medium. For example, Amiri and Vafai [23] and Amiri et al. [24] used Reynolds number and Darcy number ($= K/H^2$) to investigate the LTE assumption. Hwang

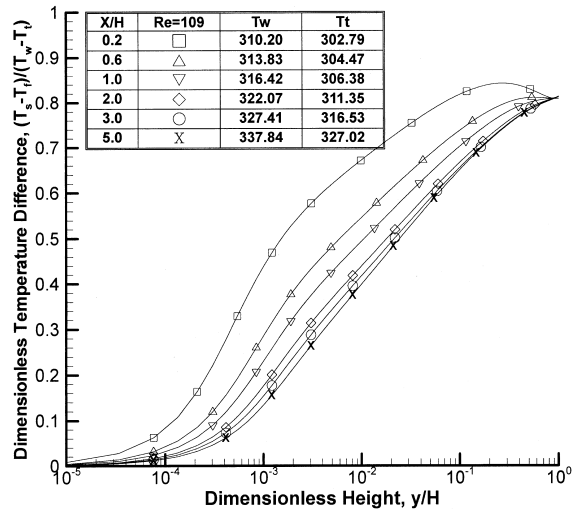


Fig. 6. Calculated dimensionless temperature difference.

and Chao [10] used Biot number ($= h_{loc}aH^2/k_s^*$) to investigate the temperature difference between the solid the fluid. In general, the trend obtained in this study is consistent with those studies.

Another important factor affecting the ratio of Nusselt number distributions calculated from one-equation and two-equation models is the Peclet number ($Pe = \rho_f u_0 C_{p_f} d/k_f$). The effect of Peclet number on the calculated Nusselt number distributions is shown in Fig. 9. It is seen that when $k_R = 5.0E - 4$, the increase in Pe will decrease the ratio of the calculated Nusselt number from the two models. This is due to the fact that as Pe is increased, the internal heat transfer between

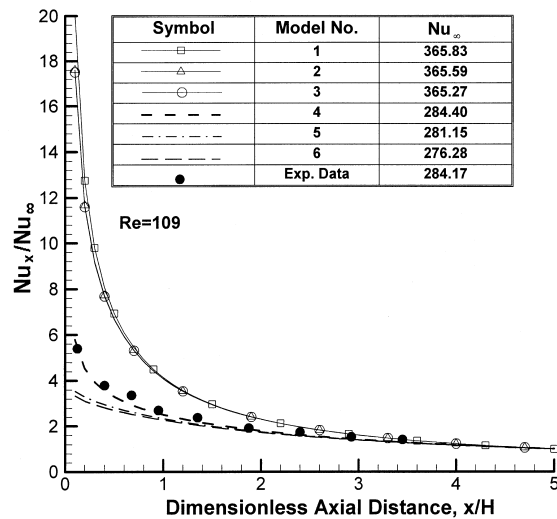


Fig. 7. Effect of different models on the calculated distribution of Nusselt number.

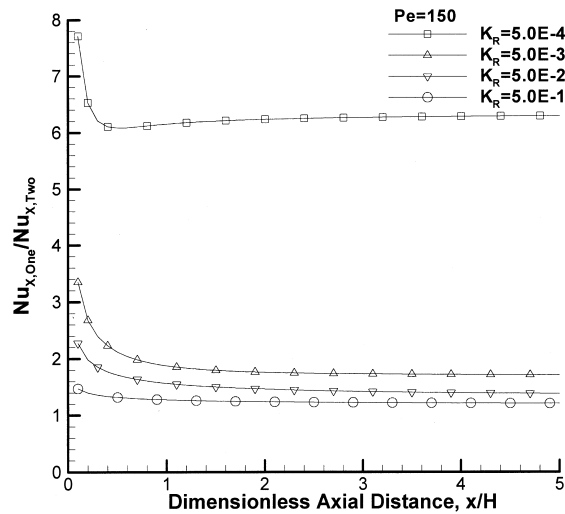


Fig. 8. Effect of thermal conductivity on the calculated distribution of Nusselt number.

the solid and the fluid increases. At $k_R = 5.0E - 4$, though Pe is increased to 400, the minimum ratio of the calculated Nusselt numbers from the two models is still greater than 2. From the calculated results, it is found that at $k_R = 5.0E - 4$, the further increase in the value of Pe from 400 to larger values would not reduce significantly the ratio of calculated Nusselt numbers. One way to further reduce the ratio is to increase the thermal conductivity ratio k_R . As shown in Fig. 9, at $Pe = 400$, when k_R is increased from $5.0E - 4$ to $5.0E - 3$, the Nusselt number ratio decreases significantly. This indicates that the K_R is a dominant factor

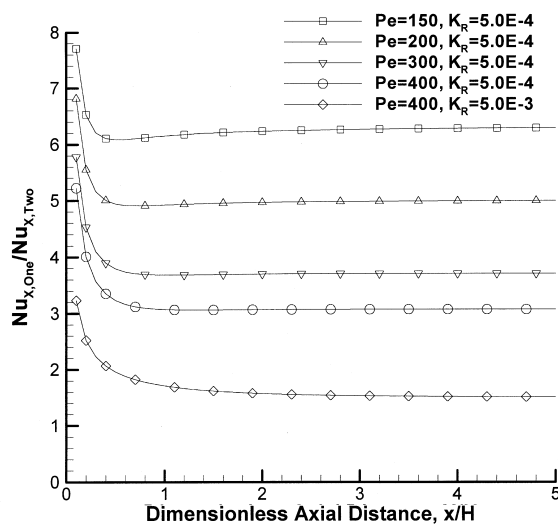


Fig. 9. Effect of Peclet number on the calculated distribution of Nusselt number.

in affecting the calculated Nusselt number ratio under the condition studied in this work.

4. Summary and conclusions

Summary and conclusions of this study are given below.

1. The heat-transfer process in the thermally developing region of a sintered bronze porous annulus is analyzed by a two-equation model to take into account the large thermal conductivity of the bronze matrix. A thermal-entrance effect function is included in the modeling of the thermal dispersion conductivity to account for the enhanced heat-transfer characteristics of the air caused by the growth of thermal boundary layer in the thermally-developing region. The empirical constants in the thermal-entrance effect function are determined by comparing the experimental data at different Reynolds numbers and heat flux conditions.
2. Due to large difference in the thermal conductivities of the bronze matrix and air, significant temperature difference between them exists in the porous annulus. The location of maximum temperature difference moves away from the heated wall along the axial direction.
3. Under the condition studied in this work, one-equation model overpredicts the Nusselt number distributions. If the thermal-entrance effect function were not included in a two-equation model, the distribution of Nusselt number would be underpredicted.
4. A parametric study is performed in this work. Results show that when the ratio of the thermal conductivity of the fluid to the solid increases, the Nusselt number distributions calculated from a one-equation model are getting closer to that from a two-equation model.

Acknowledgements

This work represents part of the results obtained under contract no. NSC-85-2622-E-194-001R sponsored by National Science Council, Taiwan, R.O.C.

References

[1] S. Bories, Natural convection in porous media, in: J. Bear, M.Y. Corapcioglu (Eds.), Advances in Transport

- Phenomena in Porous Media, Martinus Nijhoff, Dordrecht (Boston), 1987, pp. 79–141.
- [2] C.A. Coberly, W.R. Marshall, Temperature gradients in gas streams flowing through fixed granular beds, *Chem. Engng. Prog* 47 (1951) 141–150.
- [3] P. Cheng, C.T. Hsu, A. Chowdhury, Forced convection in the entrance region of a packed channel with asymmetric heating, *J. Heat Transfer* 110 (1988) 946–954.
- [4] P. Cheng, H. Zhu, Effects of radial thermal dispersion on fully-developed forced convection in cylindrical packed tubes, *Int. J. Heat Mass Transfer* 30 (1987) 2373–2383.
- [5] P. Cheng, C.T. Hsu, Applications of van Driest's mixing length theory to transverse thermal dispersion in forced convective flow through a packed bed, *Int. Commun. Heat Mass Transfer* 13 (1986) 613–625.
- [6] P. Cheng, Wall effects on fluid flow and heat transfer in porous media, *Proc. 2nd ASME/JSME Thermal Engng Joint Conf 2* (1987) 297–303.
- [7] P. Cheng, Recent studies of wall effects on fluid flow and heat transfer in packed-sphere beds, in: *Proc. Indian Congress of Appl. Mech*, 1987.
- [8] C.T. Hsu, P. Cheng, Thermal dispersion in a porous medium, *Int. J. Heat Mass Transfer* 33 (8) (1990) 1587–1597.
- [9] M.L. Hunt, C.L. Tien, Effects of thermal dispersion on forced convection in fibrous media, *Int. J. Heat Mass Transfer* 31 (2) (1988) 301–309.
- [10] G.J. Hwang, C.H. Chao, Heat transfer measurement and analysis for sintered porous channels, *J. Heat Transfer* 116 (1994) 456–464.
- [11] D.L. Koch, J.F. Brady, The effective diffusivity of fibrous media, *AIChE J* 32 (1986) 575–591.
- [12] K.K. Kar, A. Dybbs, Internal heat transfer coefficients of porous metals, in: *The Winter Annual Meeting of ASME*, Phoenix, Arizona, 1982, pp. 81–91.
- [13] J.C.Y. Koh, R. Colony, Analysis of cooling effectiveness for porous material in a coolant passage, *ASME Journal of Heat Transfer* (1974) 320–330.
- [14] D.A. Plautz, H.F. Johnstone, Heat and mass transfer in packed beds, *AIChE J* 1 (1955) 193–199.
- [15] J.H. Quinton, J.A. Storrow, Heat transfer to air flowing through packed tubes, *Chem. Engng. Sci* 5 (1956) 245–257.
- [16] K.J. Schroeder, U. Renz, K. Elegeta, *Forschungsberichte des Landes Nordrhein-Westfalen* No. 3037 (1981).
- [17] S.N. Upadhyay, B.K.D. Agarwal, D.R. Singh, On the low Reynolds number mass transfer in packed beds, *J. Chem. Eng. Jpn* 8 (1975) 413–415.
- [20] S. Whitaker, Forced convected heat transfer correlations for flow in pipes, past flat plates, single cylinders, single spheres, and for flow in packed beds and tube bundles, *AIChE J* 18 (1972) 361–371.
- [21] S. Yagi, N. Wakao, Heat and mass transfer from wall to fluid in packed beds, *AIChE J* 5 (1959) 79–85.
- [22] S. Yagi, D. Kunii, Studies on heat transfer near wall surface on packed tubes, *AIChE J* 16 (1960) 97–104.
- [23] A. Amiri, K. Vafai, Analysis of dispersion effects and non-thermal equilibrium, non-Darcian, variable porosity incompressible flow through porous medium, *Int. J. of Heat and Mass Transfer* 37 (1994) 939–954.
- [24] A. Amiri, K. Vafai, T.M. Kuzay, Effects of boundary conditions on non-Darcian heat transfer through porous media and experimental comparisons, *Numerical Heat Transfer Part I* 27 (1995) 651–664.